temperatures reached 30°C, this appears to have caused more pronounced warming of northern continents and to have led to substantial northward migration of the permafrost boundary.

Periods of Siberian speleothem growth since MIS-11 suggest a close link between greenhouse warming (hence global temperatures) and permafrost extent. After a brief hiatus in growth after MIS-11 (from 370,000 to 355,000 years ago), coinciding with a minimum in atmospheric CO<sub>2</sub> and in PWP SST during MIS-10 (Fig. 2, D and F), large thicknesses of speleothem grew in Southern Siberia during MIS-9 as greenhouse gases returned to higher values. Speleothems also grew actively during MIS-5.5 and the Holocene (>5 cm) when CO2 levels were high. In contrast, growth during MIS-7, a period of lower CO<sub>2</sub> and cooler global conditions, is minimal (maximum 1.5 cm in any studied cave), and no growth is observed during MIS-5.4 to 5.1. Conditions during MIS-7 were at the very limit for growth in southern Siberia: Speleothems grew during MIS-7.3 and 7.1 in Okhotnichya Cave (52°N) but only during MIS-7.1 just to the north at Botovskaya Cave (55°N). No growth occurred during MIS-7.5 at either cave despite higher concentrations of CO<sub>2</sub> and CH<sub>4</sub> than later in MIS-7 (26, 27) and high PWP SST (Fig. 2, D to F) (21, 22). Lake Baikal biogenic silica (24) and the percentage of arboreal pollen in Lake El'gygytgyn sediments (28) are also lower during MIS-7.5 than during MIS-7.3 and 7.1. Lower local summer insolation during MIS-7.5 (Fig. 2G) (29) suggests a role for local insolation in overprinting a Siberian climate dominantly controlled by global greenhouse gas levels.

U-Th dating of Siberian speleothem growth during recent interglacials allows detailed comparison of permafrost history with other aspects of the global climate system (Fig. 3). During MIS-5.5, speleothems started growing between 128,700 and 127,300 years ago, and this growth ended between 119,200 and 118,100 years ago (as determined from Bayesian analysis of U-Th data using OxCal-4.1; see supplementary materials). The permafrost thawing initiated when insolation was close to its maximum and greenhouse gases had just reached maximum values. Holocene permafrost degradation at our sites lags maximum insolation and greenhouse gas concentrations slightly, and starts between 10,000 and 9800 years ago. This lag may be due to the time required for permafrost to thaw at the slightly lower insolation and CO2 levels of the Holocene (relative to MIS-5.5).

Overall, dated periods of speleothem growth allow an assessment of the relationship between global temperature and permafrost extent. PWP SST was 0.5° to 1.0°C higher during MIS-5.5 and ~1.5°C higher during early MIS-11 relative to the pre-industrial Late Holocene (Fig. 2D) (21, 22). Using PWP SST as a surrogate for global temperature (21) suggests that an increase in global temperatures by 0.5° to 1.0°C will degrade only noncontinuous permafrost in southern Siberia, with the Gobi Desert remaining arid. Warming of ~1.5°C (i.e., as in MIS-11) may cause a substantial thaw of continuous permafrost as far north as 60°N and may create wetter conditions in the Gobi Desert. Such warming is therefore expected to markedly change the environment of continental Asia and can potentially lead to substantial release of carbon trapped in the permafrost into the atmosphere.

# References and Notes

- 1. G. Grosse et al., EOS 92, 73 (2011).
- 2. E. A. G. Schuur et al., Bioscience 58, 701 (2008).
- 3. O. Anisimov, S. Reneva, AMBIO 35, 169 (2006).
- 4. V. E. Romanovsky, S. L. Smith, H. H. Christiansen, Permafr. Periglac. Proc. 21, 106 (2010).
- 5. Y. K. Vasil'chuk, J.-C. Kim, A. C. Vasil'chuk, Nucl. Instrum. Methods Phys. Res. B 223-224, 650 (2004).
- 6. D. A. Gilichinsky et al., Quat. Sci. Rev. 26, 1547 (2007).
- 7. H. P. Schwarcz, in Handbook of Environmental Isotope Geochemistry, P. Fritz, J. C. Fontes, Eds. (Elsevier, Amsterdam, 1986), vol. 2, pp. 271-300.
- 8. R. A. Cliff, C. Spötl, A. Mangini, Quat. Geochronol. 5, 452
- 9. B. Lauriol, D. C. Ford, J. Cinq-Mars, W. A. Morris, Can. J. Earth Sci. 34, 902 (1997).
- 10. S. E. Lauritzen, Quat. Res. 43, 133 (1995).
- 11. A. Vaks, M. Bar-Matthews, A. Matthews, A. Ayalon, A. Frumkin, Quat. Sci. Rev. 29, 2647 (2010).
- 12. Philip's Modern School Atlas, 95th Edition (Philip's/Octopus, London, 2007).
- 13. A. Jones et al., Eds., Soil Atlas of the Northern Circumpolar Region (Publication Office of the European Union, Luxembourg, 2010).
- 14. D. Dorjotov, N. Orshikh, T. Oyunchimeg, Geographic Atlas of Mongolian Republic (Mongolian Institute of Geodesy and Cartography, Ulaanbaatar, 2004). [in Mongolian]
- 15. N. Wu et al., Quat. Sci. Rev. 26, 1884 (2007).
- 16. A. W. Mackay et al., J. Quat. Sci. 23, 365 (2008).
- 17. A. de Vernal, C. Hillaire-Marcel, Science 320, 1622 (2008).
- 18. J. F. McManus, D. W. Oppo, J. L. Cullen, Science 283, 971 (1999)
- 19. M. E. Raymo, J. X. Mitrovica, Nature 483, 453 (2012).
- 20. L. Ortlieb, A. Diaz, N. Guzman, Quat. Sci. Rev. 15, 857 (1996).
- 21. ]. Hansen et al., Proc. Natl. Acad. Sci. U.S.A. 103, 14288 (2006).

- 22. M. Medina-Elizalde, D. W. Lea, Science 310, 1009 (2005).
- 23. A. J. Dickson et al., Nat. Geosci. 2, 428 (2009).
- 24. A. A. Prokopenko et al., Quat. Res. 55, 123 (2001).
- 25. M. Melles et al., Science 337, 315 (2012).
- 26. L. Loulerque et al., Nature 453, 383 (2008).
- 27. D. Lüthi et al., Nature 453, 379 (2008).
- 28. N. R. Nowaczyk et al., Geophys. J. Int. 150, 109 (2002). 29. J. Laskar et al., Astron. Astrophys. 428, 261 (2004).
- 30. J. Brown, O. J. Ferrians Jr., J. A. Heginbottom, E. S. Melnikov, Circum-Arctic Map of Permafrost and Ground Ice Conditions (National Snow and Ice Data Center/World Data Center for Glaciology, Boulder, CO, 2001).
- 31. L. E. Lisiecki, M. E. Raymo, Paleoceanography 20, PA1003 (2005).
- 32. Y. Wang et al., Nature 451, 1090 (2008).
- 33. S. O. Rasmussen et al., I. Geophys. Res. 111, D06102 (2006).
- 34. See references 16 to 19 in the supplementary materials.

Acknowledgments: This article is dedicated to the memory of Prof. Y. Trzhcinski, who during the last months of his life made a big effort to establish the cooperation between the University of Oxford and Institute of Earth's Crust (IEC) in Irkutsk. We thank D. Sokolnikov and other "Arabica" members, E. Kozireva (IEC), V. Alexioglo, and V. Balaev from Lensk for their help during the fieldwork in Siberia; the Mongolian Speleological Society for their help with the fieldwork in Mongolia: 1. Fritz and L. Zehnder (ETH Zürich) for preparing Fig. 1 and for assistance with XRD analyses, respectively; and C. Day, V. Ersek, L. Zanna, P. Holdship, O. Green, S. Wyatt, Y. Nakajima, P. Pousada Solino, J. Cox, S. Usher, M. Chung, and others from University of Oxford for the help with the laboratory work, administration and computing issues, obtainment of funding, and fruitful discussions. Supported by NERC Fellowship NE/G013829/1, Royal Society grant JP080831, and Russian Foundation for Basic Research joint grant 09-05-92605 KO\_a.

# Supplementary Materials

www.sciencemag.org/cgi/content/full/science.1228729/DC1 Materials and Methods

Supplementary Text

Figs. S1 to S16

Tables S1 to S3 References

13 August 2012; accepted 6 February 2013 Published online 21 February 2013;

10.1126/science.1228729

# A Long-Lived Relativistic Electron Storage Ring Embedded in Earth's **Outer Van Allen Belt**

D. N. Baker, 1\* S. G. Kanekal, V. C. Hoxie, M. G. Henderson, X. Li, H. E. Spence, 4 S. R. Elkington, R. H. W. Friedel, J. Goldstein, M. K. Hudson, G. D. Reeves, R. M. Thorne, 7 C. A. Kletzing, 8 S. G. Claudepierre 9

Since their discovery more than 50 years ago, Earth's Van Allen radiation belts have been considered to consist of two distinct zones of trapped, highly energetic charged particles. The outer zone is composed predominantly of megaelectron volt (MeV) electrons that wax and wane in intensity on time scales ranging from hours to days, depending primarily on external forcing by the solar wind. The spatially separated inner zone is composed of commingled high-energy electrons and very energetic positive ions (mostly protons), the latter being stable in intensity levels over years to decades. In situ energy-specific and temporally resolved spacecraft observations reveal an isolated third ring, or torus, of high-energy (>2 MeV) electrons that formed on 2 September 2012 and persisted largely unchanged in the geocentric radial range of 3.0 to ~3.5 Earth radii for more than 4 weeks before being disrupted (and virtually annihilated) by a powerful interplanetary shock wave passage.

The magnetically confined radiation zones surrounding Earth were the first major discovery of the Space Age in 1958 (1-4).

Long-term observations of these energetic particle populations have subsequently shown dramatic, highly dynamic changes of the outer Van Allen belt. Previous, rather sparse measurements of the radiation environment suggested that powerful acceleration events for relativistic electrons occur on time scales ranging from minutes (5, 6) to many hours (7, 8). Thus, there has been direct, as well as circumstantial evidence that an immensely powerful and efficient accelerator operates within the terrestrial magnetosphere just a few thousand kilometers above Earth's surface.

On 30 August 2012, twin NASA spacecraft, the Radiation Belt Storm Probes (RBSPs), were launched into highly elliptical, low-inclination orbits around Earth. The RBSP satellites are fully instrumented with identical energetic particle, plasma, magnetic field, and plasma wave sensors to measure and thoroughly characterize the radiation belt regions (9). The scientific payloads on board the RBSP spacecraft (renamed the "Van Allen Probes mission" by NASA at a formal ceremony on 9 November 2012) have unprecedented detection sensitivity, energy resolution, and temporal sampling capability. In particular, the Relativistic Electron-Proton Telescope (REPT) experiment (10) measures the key  $\sim$ 1- to  $\sim$ 20-MeV electron population throughout the RBSP orbit, which extends from geocentric distances of radius  $r = 1.2R_E$  to  $5.8R_E$  ( $R_E$ : Earth radius = 6372 km). The REPT sensors were among the first instruments turned on and have been return-

<sup>1</sup>Laboratory for Atmospheric and Space Physics, University of Colorado, Boulder, CO, USA. <sup>2</sup>Goddard Space Flight Center, Greenbelt, MD, USA. <sup>3</sup>Los Alamos National Laboratory, Los Alamos, NM, USA. <sup>4</sup>Institute for the Study of Earth, Oceans, and Space, University of New Hampshire, Durham, NH, USA. <sup>5</sup>Space Science and Engineering Division, Southwest Research Institute, San Antonio, TX, USA. <sup>6</sup>Department of Physics and Astronomy, Dartmouth College, Hanover, NH, USA. <sup>7</sup>Department of Atmospheric and Oceanic Sciences, University of California—Los Angeles, Los Angeles, CA, USA. <sup>8</sup>Department of Physics and Astronomy, University of Iowa, Iowa City, IA, USA. <sup>8</sup>The Aerospace Corporation, Los Angeles, CA, USA.

\*Corresponding author. E-mail: daniel.baker@lasp.colorado.edu

ing nearly continuous data from both Van Allen Probes spacecraft since 1 September 2012.

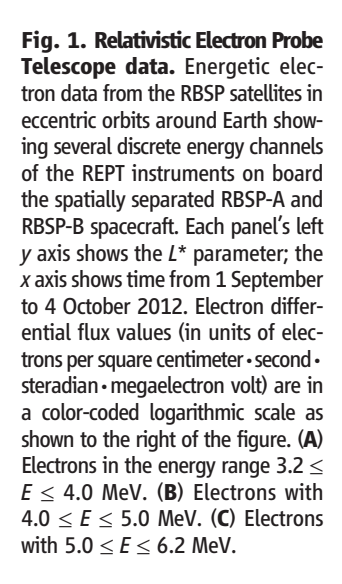
Prior key measurements of Earth's radiation environment have been made (11-13), but some of the longest and most comprehensive radiation belt observations have previously come from sensors on board the Solar, Anomalous, and Magnetospheric Particle Explorer (SAMPEX) mission (14). This spacecraft made low-Earth orbit observations of inner- and outer-zone particles from its launch in July 1992 until its recent atmospheric reentry and demise on 13 November 2012 (15, 16). SAMPEX measured energy E > 1 MeV electrons at the near-Earth foot of magnetic field lines but was never able to look into the "throat" of the radiation belt accelerator in the magnetospheric equatorial plane. This contrasts dramatically with the REPT-A and REPT-B instrument data collected by the Van Allen Probes from 1 September 2012 through early October 2012 (Fig. 1). These data show that a powerful electron acceleration event was already in progress when the instruments were first turned on. The entire outer radiation belt was enhanced in electron flux from  $E \sim 3.0$  MeV (Fig. 1A) up to energies well above the  $5.0 \le E \le 6.2$  MeV channel (Fig. 1C). At this time, the radiation belt populations clearly had the expected double-belt structure with an inner zone, an outer zone, and a "slot" region of greatly diminished intensity separating the two.

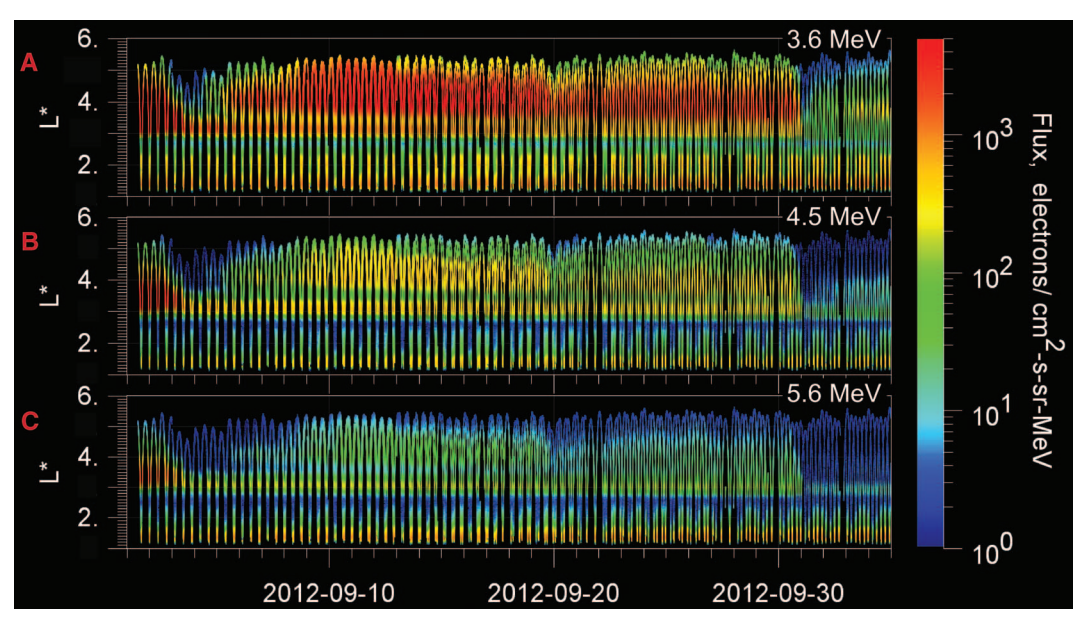
What is most notable (and unexpected) is the clear emergence of a separate, previously unseen belt, or "storage ring," of high-energy electrons that stands out clearly after 2 September 2012. This belt is evident in the E=4.0 to 5.0 MeV range (Fig. 1B) and is the dominant flux feature in the E=5.0 to 6.2 MeV energy range (Fig. 1C). This distinctive ring of highly relativistic electrons persists, changing only gradually, until its abrupt and almost complete disappearance late on 1 October 2012. Though the inner zone, the

slot region, and the relativistic storage ring (3.0 <  $L^* < \sim 3.5$ , where  $L^*$  is the distance in Earth radii at which a magnetic field line crosses the magnetic equatorial plane) change relatively little over this 4-week period, the more distant part of the outer Van Allen belt shows huge dynamical changes with new electron populations appearing at  $L^* > 4.0$ , beginning on ~7 September and intensifying greatly over a period of 2 weeks. Subsequently, the outermost parts of the outer Van Allen zone grew and diminished further with little effect on the storage-ring feature until the abrupt demise of virtually the entire outer-zone electron population at the end of 1 October. Other electron sensor systems on board the Van Allen Probes spacecraft, overlapping partially in energy coverage with the REPT sensors, also detected the storage-ring feature (17).

The distinct storage-ring feature is more clearly evident in the meridional plane projection of 4.0-to 5.0-MeV electrons from the combined REPT-A and REPT-B instrument records (Fig. 2). In the earliest observational phase (1 to 3 September 2012), the expected two-belt structure of the Van Allen zones is clear (Fig. 2A). In the next phase from 3 to 6 September, the relativistic storage ring was formed (Fig. 2B), probably largely by erosion and loss of the more distant parts of the outer zone. The storage ring persisted in a notably stable fashion (Fig. 2, C and D) throughout the remainder of September until its almost complete annihilation in early October 2012.

Instruments on board the Combined Release and Radiation Effects Satellite (CRRES) spacecraft (13) observed a powerful "injection" of highenergy electrons and protons deep into the inner part of Earth's magnetosphere on 24 March 1991 (5, 18, 19). This was a highly impulsive event caused by an exceptionally strong interplanetary shock wave (5, 6). This event is a stark example of the sudden appearance of a newly energized



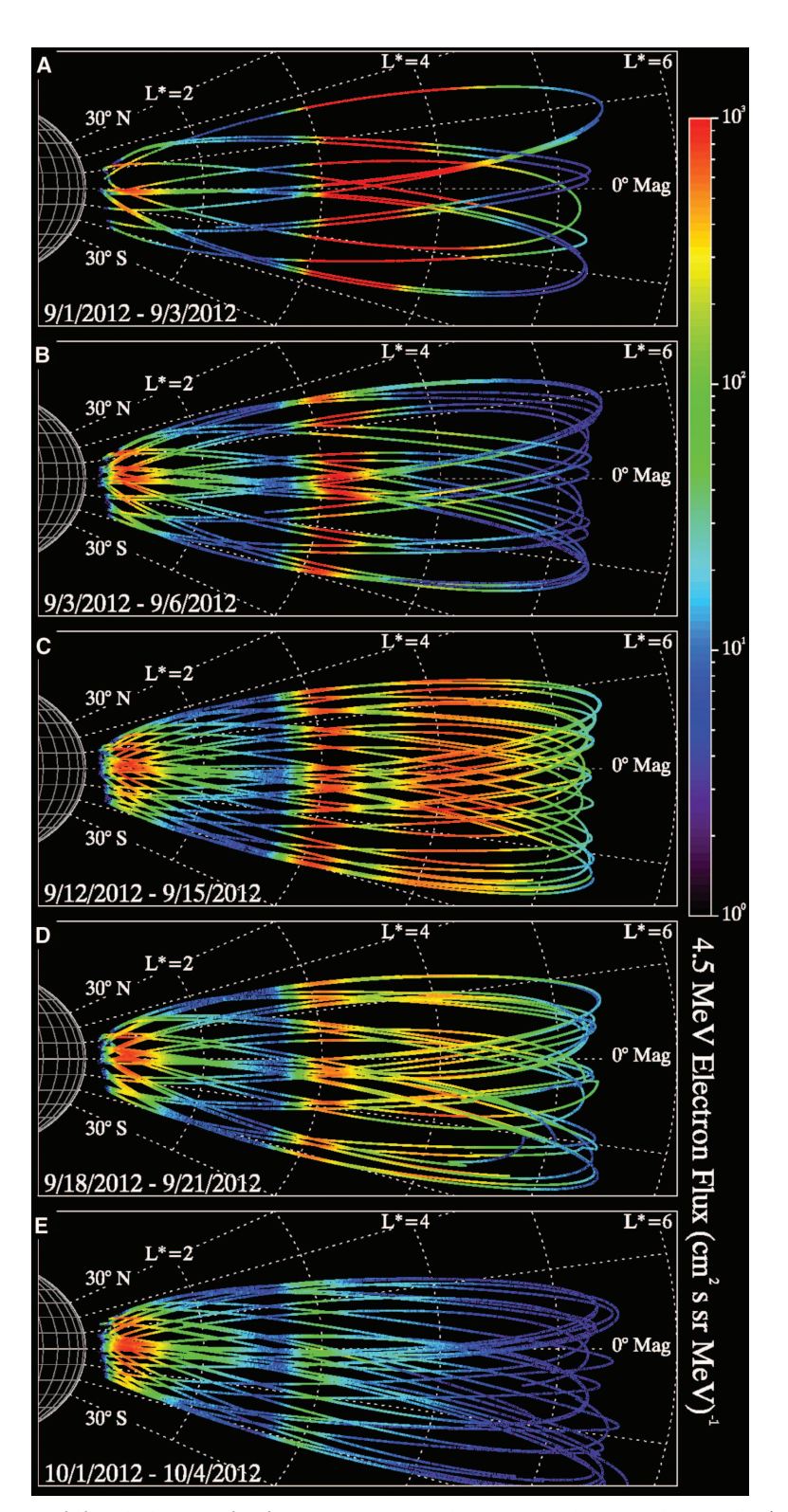


population of both protons and electrons in a localized portion of the slot region of the radiation belts that is normally almost devoid of very energetic particles (19, 20). Moreover, this prior event contrasts with the storage-ring feature observed by the Van Allen Probes sensors: The storage ring clearly resulted largely from loss of the more distant portion of the outer-zone electron population rather than fresh, localized injection of the March 1991 type. The original acceleration of the electron population (before the turn-on of REPT on 1 September 2012) that eventually formed the storage ring may have resulted from local wave heating (21, 22), enhanced radial diffusion (23, 24), or both.

Based on prior radiation belt research [e.g., (7, 15)], the outer Van Allen zone electron populations would be expected to respond rather directly to changes in the solar wind, interplanetary magnetic field (IMF), and geomagnetic activity. The development of the storage-ring feature itself (Fig. 3) was closely associated with the loss of outer-belt electrons after passage of an interplanetary shock wave on 3 September 2012, seen as a sharp increase in solar wind speed (Fig. 3B) and abrupt change in the IMF (Fig. 3C). Subsequently, a new population of highly relativistic electrons emerged at a region around  $L^* \sim 4.0$  and grew in intensity and spatial extent (Fig. 3A) after a high-speed solar wind episode (Fig. 3B) on 5 September. Another such period of high-energy electron flux diminution, reappearance, and intensification was seen from ~21 September to 1 October 2012 (Fig. 3A), with this sequence again occurring in the wake of a powerful highspeed solar wind stream on 20 to 21 September (Fig. 3B). As noted above, one of the most abrupt and notable features of the entire data set was the nearly complete disappearance of the entire outer-zone electron population late on 1 October associated with another interplanetary shock wave (Fig. 3, B and C) and relatively strong geomagnetic storm [seen in disturbance storm time (Dst), which measures global magnetic field disturbance (Fig. 3D)].

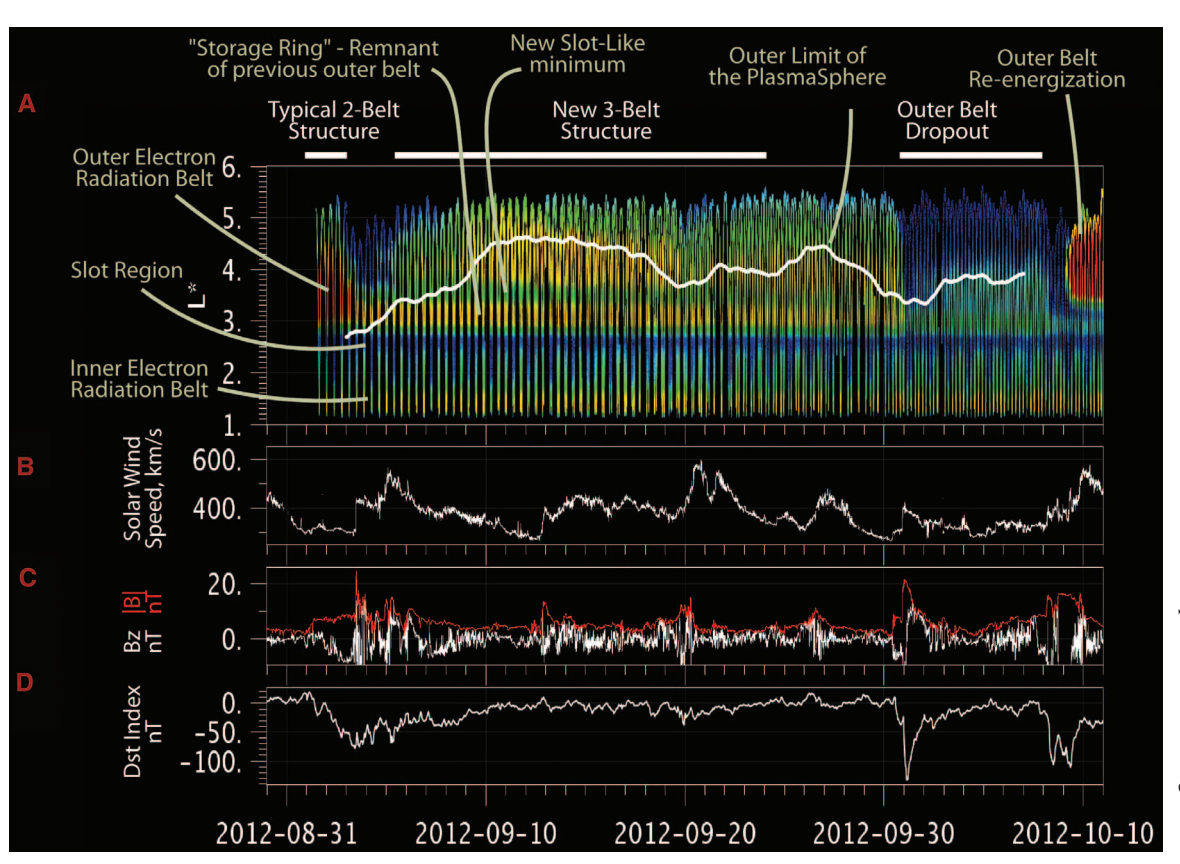
Figure 3A shows that for the period of 1 to 4 September 2012, the average plasmapause boundary was relatively close to Earth ( $L^* \sim 3$ ), and a powerful outer-zone electron acceleration event was occurring in the low–plasma-density region outside the plasmasphere. However, from  $\sim$ 4 September until  $\sim$ 6 October, the plasmapause was much farther outward, around  $L^* > 4$ . Thus, the storage-ring feature, as well as most of the outer Van Allen zone E > 4.5 MeV electron population, was inside the high-density plasmasphere. However, in the traditional picture, the outer-zone electron belt would be largely outside the plasmasphere, and the slot region would be inside the plasmasphere outer boundary (21-23, 25).

The radiation belt particle populations are determined by a complex superposition of acceleration, transport, and loss processes modulated by their interactions with plasma waves (24). We are now seeing unexpected radiation



**Fig. 2. Meridional plane projections.** Projections of the REPT-A and REPT-B electron flux (4.0 to 5.0 MeV) values, as shown according to the logarithmic color scale to the right of the figure. Each panel shows a limited interval of time in a magnetic latitude  $L^*$  coordinate system. (**A**) For 1 to 3 September 2012, the expected two-belt Van Allen zone structure consists of an inner-zone electron population ( $L^* < \sim 2.5$ ), a relatively empty slot region (2.5 <  $L^* < 3.0$ ), and an outer-zone population ( $L^* > 3.0$ ). (**B**) From 3 to 6 September, only an intense belt of electrons remains in the range  $3.0 < L^* < 3.5$ ; the inner zone and traditional slot region have not changed. (**C**) The storage-ring belt, or torus, feature persists at  $3.0 < L^* < 3.5$ , whereas a new slot region is seen at  $3.5 < L^* < 3.8$ , and a completely new outer-zone population has formed at  $L^* > 3.8$ . (**D**) The storage-ring feature remains, whereas the outer zone at  $L^* > 3.8$  decays away. (**E**) The entire outer zone ( $L^* > \sim 3.0$ ) has virtually disappeared at these energies.

Fig. 3. Development of the storage ring. (A) Image similar to Fig. 1B. but also including the plasmapause, the outer boundary of the plasmasphere (26) for the period 1 September to 7 October 2012. The white curve overplotted on the colorcoded electron particle flux data in Fig. 3A shows the modeled, 3-day averaged plasmapause radial location that is in agreement with concurrent plasma wave data (17, 27, 28). (B) Concurrently measured solar wind speed upstream of Earth's magnetosphere. (C) Interplanetary magnetic field for the interval under study. |B|, the magnitude of the interplanetary magnetic field components parallel to the ecliptic in nanotesla (nT); B<sub>z</sub>, the values of the components perpendicular. (D) Geomagnetic activity index (Dst) for the period under study.



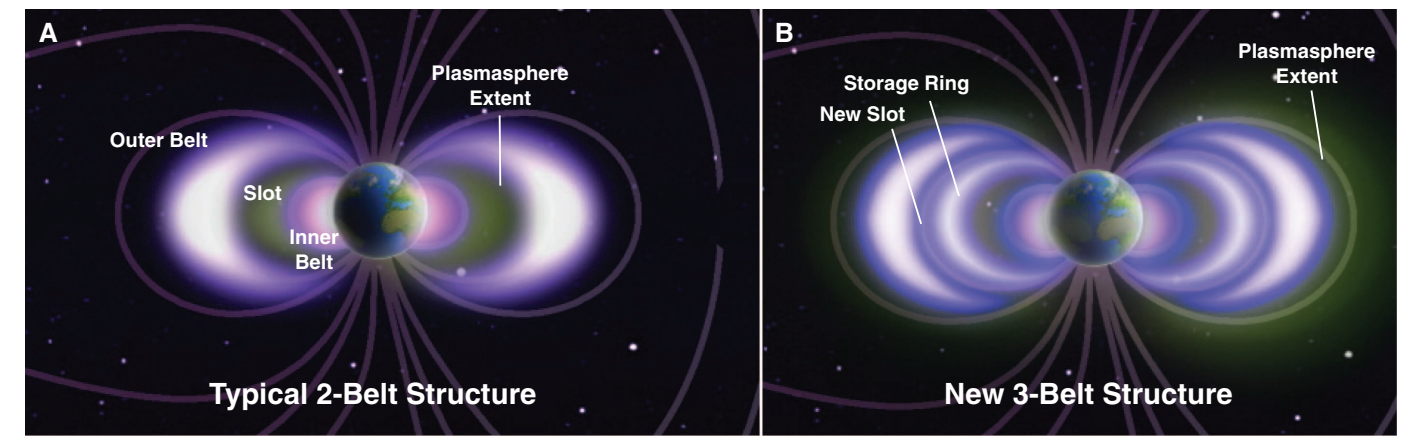


**Fig. 4. Radiation belt structures.** Diagrams providing a cross-sectional view of Earth's radiation belt structure and relation to the plasmasphere. (A) Schematic diagram showing Earth, the outer and inner radiation belts, and the normal plasmaspheric location. (B) Similar to (A), but showing a more highly distended plasmasphere and unexpected triple radiation belt

properties during the September 2012 period. The radiation belts are really "doughnut-" or torus-shaped entities in three dimensions. Earth is portrayed at the center. White denotes the highest electron fluxes; blue indicates the lowest fluxes. The translucent green overlay denotes the plasmasphere.

belt structures (Fig. 4), but have yet to fully understand them in the context of present radiation belt theory.

### **References and Notes**

- 1. J. A. Van Allen et al., Jet Propuls. 28, 588 (1958).
- 2. J. A. Van Allen, J. Geophys. Res. 64, 1683 (1959).
- 3. 1. A. Van Allen, L. A. Frank, *Nature* **183**, 430 (1959).
- 4. S. C. Freden, R. S. White, Phys. Rev. Lett. 3, 9 (1959).
- J. B. Blake, W. A. Kolasinski, R. W. Fillius, E. G. Mullen, Geophys. Res. Lett. 19, 821 (1992).
- 6. X. Li et al., Geophys. Res. Lett. 20, 2423 (1993).

- 7. D. N. Baker et al., Geophys. Res. Lett. 21, 409 (1994).
- 8. R. B. Horne *et al., J. Geophys. Res.* **110**, A03225 (2005). 9. B. H. Mauk *et al., Space Sci. Rev.* 10.1007/s11214-012-
- 9908-y (2012). 10. D. N. Baker *et al.*, *Space Sci. Rev.* 10.1007/s11214-012-9950-9 (2012)
- 11. Since the initial Van Allen belt discovery, there have been many missions that have measured key aspects of the radiation properties around Earth. Some of these have been from operational satellite systems such as the National Oceanic and Atmospheric Administration weather satellites in geostationary Earth orbit (GEO) (www.oso.noaa.gov/qoesstatus) or polar low-Earth

(www.oso.noaa.gov/poesstatus) orbits. Other measurements have been made using sensors on board operational GEO spacecraft or the Global Positioning Satellite timing and navigation constellation of spacecraft, as well as the Polar and Cluster scientific satellites (12). These prior satellites have provided key long-term monitoring of radiation belt changes, but have generally not made measurements directly in the heart of the radiation belt regions. Only the CRRES mission (13) operated briefly (1990 to 1991) in the heart of the radiation belts, but this mission lacked the background rejection and the temporal, energy, and spatial resolution now provided by the dual Van Allen Probes.

- 12. R. H. W. Friedel, G. D. Reeves, T. Obara, J. Atmos. Sol. Terr. Phys. 64, 265 (2002).
- 13. M. H. Johnson, J. Kierein, J. Spacecr. Rockets 29, 556
- 14. D. N. Baker et al., IEEE Trans. Geosci. Rem. Sens. 31. 531 (1993).
- 15. X. Li, M. Temerin, D. N. Baker, G. D. Reeves, J. Geophys. Res. 116, A11207 (2011).
- 16. D. N. Baker, J. E. Mazur, G. M. Mason, Space Weather 10, 505006 (2012).
- 17. See data and methods in the accompanying supplementary materials on Science Online.
- 18. A. L. Vampola, A. Korth, Geophys. Res. Lett. 19, 625 (1992).
- 19. E. G. Mullen, M. S. Gussenhoven, K. Ray, M. Violet, IEEE Trans. Nucl. Sci. 38, 1713 (1991).
- 20. D. H. Brautigam, JASTP 64, 1709 (2002).
- 21. R. B. Horne et al., Nature 437, 227 (2005).

- 22. Y. Y. Shprits et al., Geophys. Res. Lett. 33, L05104 (2006).
- 23. X. Li, D. N. Baker, T. P. O'Brien, L. Xie, Q. G. Zong, Geophys. Res. Lett. 33, L14107 (2006).
- 24. R. M. Thorne, Geophys. Res. Lett. 37, L22107 (2010)
- 25. L. R. Lyons, R. M. Thorne, J. Geophys. Res. 78, 2142 (1973)
- 26. J. Goldstein, Space Sci. Rev. 124, 203 (2006).
- 27. J. Goldstein, B. R. Sandel, W. T. Forrester, M. F. Thomsen, M. R. Hairston, J. Geophys. Res. 110, A12218
- 28. R. E. Denton et al., J. Geophys. Res. 117, A03221

Acknowledgments: This work was supported by RBSP-Energetic Particle Composition and Thermal Plasma Suite funding provided by the Johns Hopkins

University Applied Physics Laboratory (JHU/APL) contract no. 967399, Electric and Magnetic Field Instrument Suite and Integrated Science (EMFISIS) work was supported on JHU/APL contract no. 921649, and both were funded under NASA's Prime contract no. NAS5-01072. All Van Allen Probes observations used in this study, along with display and analysis software, are publicly available at the Web site www.rbsp-ect.lanl.gov.

#### Supplementary Materials

www.sciencemag.org/cgi/content/full/science.1233518/DC1 Supplementary Text Figs. S1 and S2

3 December 2012; accepted 5 February 2013 Published online 28 February 2013; 10.1126/science.1233518

# A Guanosine-Centric Mechanism for RNA Chaperone Function

Jacob K. Grohman, <sup>1,2</sup> Robert J. Gorelick, <sup>5</sup> Colin R. Lickwar, <sup>3</sup> Jason D. Lieb, <sup>3</sup> Brian D. Bower, <sup>4</sup> Brent M. Znosko, <sup>6</sup> Kevin M. Weeks <sup>1</sup>\*

RNA chaperones are ubiquitous, heterogeneous proteins essential for RNA structural biogenesis and function. We investigated the mechanism of chaperone-mediated RNA folding by following the time-resolved dimerization of the packaging domain of a retroviral RNA at nucleotide resolution. In the absence of the nucleocapsid (NC) chaperone, dimerization proceeded through multiple, slow-folding intermediates. In the presence of NC, dimerization occurred rapidly through a single structural intermediate. The RNA binding domain of heterogeneous nuclear ribonucleoprotein A1 protein, a structurally unrelated chaperone, also accelerated dimerization. Both chaperones interacted primarily with guanosine residues. Replacing guanosine with more weakly pairing inosine yielded an RNA that folded rapidly without a facilitating chaperone. These results show that RNA chaperones can simplify RNA folding landscapes by weakening intramolecular interactions involving guanosine and explain many RNA chaperone activities.

utside the cellular environment or in the absence of chaperone proteins, most RNAs fold via complex pathways involving multiple, long-lived intermediates. RNA chaperone proteins with non- or semispecific RNA binding activities accelerate adoption of the thermodynamically most stable RNA structure by lowering the energetic barriers between RNA states and by facilitating rearrangement of misfolded states (1-4). Retroviruses package two RNA genomes in each virus particle (5). These genomes dimerize near their 5' ends, and dimerization is catalyzed by an RNA chaperone, nucleocapsid (NC), which is derived from the retroviral Gag protein that coassembles with the viral RNA to generate replication-competent virus (2, 6, 7). By

of 46 and 115 nucleotides, respectively. This RNA dimerizes under physiological-like conditions

following the dimerization of a region of the

Moloney murine leukemia virus (MuLV) genomic

RNA at single-nucleotide resolution, we uncovered

a simple mechanism for how a retroviral nucleo-

170-nucleotide (nt) MuLV dimerization region

(8–10) and including 5' and 3' flanking sequences

We studied an RNA construct spanning the

capsid chaperone protein functions.

USA. <sup>3</sup>Department of Biology and Carolina Center for Genome Sciences, University of North Carolina, Chapel Hill, NC 27599, USA. <sup>4</sup>Department of Genetics, University of North Carolina, Chapel Hill, NC 27599, USA. 5AIDS and Cancer Virus Program, SAIC-Frederick, Inc., Frederick National Laboratory for Cancer Research, Frederick, MD 21702–1201, USA. <sup>6</sup>Department of Chemistry, Saint Louis University, Saint Louis, MO 63103, USA.

<sup>1</sup>Department of Chemistry, University of North Carolina, Chapel

Hill, NC 27599-3290, USA. <sup>2</sup>Department of Biochemistry and

Biophysics, University of North Carolina, Chapel Hill, NC 27599,

in vitro and has a structure similar to that of genomic RNA isolated from virions (11, 12). Point mutations in this region of the MuLV genome eliminate its selective packaging into virions (10). We followed dimerization at single-nucleotide resolution using time-resolved, selective 2'-hydroxyl acylation analyzed by primer extension (SHAPE) (13, 14). A fast-acting reagent, benzoyl cyanide (BzCN), that either reacts to form a 2'-O-adduct at conformationally flexible nucleotides or undergoes rapid self-inactivation by hydrolysis (with a 0.25-s half-life), was used (14). Each time point, obtained over reactions spanning tens of minutes,

SHAPE profiles for the initial monomer and final dimer forms agree well with accepted structures for the MuLV dimerization domain (fig. S1

thus yields a structural snapshot of  $\sim 1$  s duration.

and text S1). Five key regions underwent largescale structural changes during dimerization (Fig. 1). The loops of hairpins SL1 and SL2 (positions 329 to 332 and 363 to 366, respectively) were reactive in the monomer and became unreactive during dimerization (within 7 s), consistent with formation of a stable intermolecular loop-loop kissing interaction (15). Two palindromic sequences, PAL1 (positions 210 to 219) and PAL2 (positions 283 to 298), were initially reactive but became unreactive because of intermolecular duplex formation in the dimer. Conversely, two regions that form the "anchoring helix" (positions 231 to 251 and 290 to 315) in the monomer became more reactive upon dimer formation (Fig. 1 and fig. S1).

We obtained SHAPE data for every nucleotide within the 170-nt MuLV domain in 16 1-s snapshots yielding more than 2700 structural data points. We grouped nucleotides with similar kinetic behaviors by k-means clustering (16). In the presence of 5 mM Mg<sup>2+</sup> and without a protein chaperone, there were seven distinct kinetic behaviors involving four net rates (Fig. 2A). Rates were identical, within error, over a three-fold change in RNA concentration (fig. S2), indicating that most conformational changes reflect pseudo-unimolecular transitions between two interacting RNAs. The fastest rate of  $\geq 5 \text{ min}^{-1}$  (Fig. 2A; cluster 1a, in orange on structures at bottom) occurred at nucleotides at the apexes of SL1 and SL2, suggesting formation of a complex between two RNAs before the first time point. PAL1 nucleotides became less reactive at a net rate of  $1.6 \pm 0.4 \text{ min}^{-1}$  (Fig. 2A, cluster 1b, green on structures). The anchoring helix and PAL2 nucleotides demonstrated opposing kinetic behaviors (rates of  $0.30 \pm 0.03 \text{ min}^{-1}$ ) (Fig. 2A, clusters 2 and 3, in red), suggestive of a single process involving both structures. Positions in a large, flexible domain (positions 251 to 282) showed slower kinetic behavior with a net rate of 0.11  $\pm$ 0.02 min<sup>-1</sup> (Fig. 2A, cluster 4, in black on structures). Finally, nucleotides in clusters 5 and 6 showed biphasic kinetic behavior in which the SHAPE reactivity first increased and then decreased over time, or vice versa, with rates of 1.6 and 0.1 min<sup>-1</sup>. Time-resolved SHAPE anal-

<sup>\*</sup>Corresponding author. E-mail: weeks@unc.edu



# A Long-Lived Relativistic Electron Storage Ring Embedded in Earth's Outer Van Allen Belt

D. N. Baker, S. G. Kanekal, V. C. Hoxie, M. G. Henderson, X. Li, H. E. Spence, S. R. Elkington, R. H. W. Friedel, J. Goldstein, M. K. Hudson, G. D. Reeves, R. M. Thorne, C. A. Kletzing, and S. G. Claudepierre

Science 340 (6129), . DOI: 10.1126/science.1233518

# Van Allen Variation

The two rings of relativistic particles called Van Allen Belts that encircle Earth were discovered during the space age, and are known to pose risks to satellites in geostationary orbit. NASA launched twin spacecraft, the Van Allen Probes, on 30 August 2012 to measure and characterize Earth's radiation belt regions. **Baker et al.** (p. 186, published online 28 February) have shown that a third, unexpected and temporary, radiation belt formed on 2 September 2012 to disappear 4 weeks later in response to changes in the solar wind.

# View the article online

https://www.science.org/doi/10.1126/science.1233518

**Permissions** 

https://www.science.org/help/reprints-and-permissions

Use of this article is subject to the Terms of service